THE JOURNAL OF PHYSICAL CHEMISTRY C

Article

Cite This: J. Phys. Chem. C 2018, 122, 27597−27607

pubs.acs.org/JPCC

Correlation between Structure, Chemistry, and Dielectric Properties of Iron-Doped Gallium Oxide ($Ga_{2-x}Fe_xO_3$)

Swadipta Roy,[†,‡] B. Mallesham,[†] Vishal B. Zade,[†] Abraham Martinez,[§] V. Shutthanandan,[§] S. Thevuthasan,[§] and C. V. Ramana*[,†]

[†]Center for Advanced Materials Research (CMR) and [‡]Department of Metallurgical, Materials and Biomedical Engineering, University of Texas at El Paso, 500 W University Avenue, El Paso, Texas 79968, United States

[§]Environmental Molecular Sciences Laboratory (EMSL), Pacific Northwest National Laboratory (PNNL), Richland, Washington 99352, United States

ABSTRACT: Iron (Fe)-doped gallium oxide (Ga_2O_3) compounds ($Ga_{2-x}Fe_xO_3$; x = 0.0−0.3; referred to GFO) were synthesized by the standard high-temperature solid-state chemical reaction method. X-ray diffraction analyses confirmed that the sintered GFO compounds stabilized in monoclinic crystal structure with $C2/m$ space group. Local structure and chemical bonding analyses using XANES revealed that the Fe occupies octahedral and tetrahedral sites similar to Ga in parent Ga_2O_3 lattice without considerable changes in the local symmetry. Morphology of the GFO compounds is characterized by the presence of rod-shaped particle (from around 2.0−3.5 μm) features. The energy dispersive X-ray spectroscopy confirmed the chemical stoichiometry of the GFO compounds, where the atomic ratio of the constituted elements is in accordance with the calculated concentration values. The frequency- and temperature-dependent dielectric properties of the GFO compounds exhibited the traditional dielectric dispersion behavior. Relatively high dielectric constant at lower frequencies is attributed to Maxwell−Wagner type of dielectric relaxation, which primarily originated from uncompensated charges at electrode material interface. On the basis of the results and analyses, the effect of Fe content on the crystal structure, chemical bonding and local structure, and dielectric properties of $Ga_{2-x}Fe_xO_3$ compounds is established.

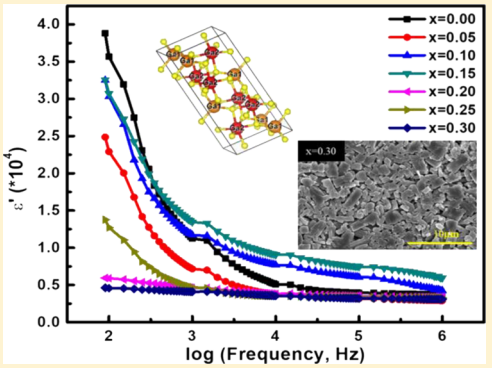

1. INTRODUCTION

Wide band gap oxide dielectrics, such as ZrO_2, HfO_2, Ga_2O_3, and La_2O_3 and chemical compounds based on these materials, are of continued recent interest because of their excellent electronic properties, optical phenomena, and technological applications such as in microelectronics, low-loss dielectric nanoantennas, field effect transistors, and complementary metal-oxide-semiconductors.[1−10] Ga_2O_3, one among these oxide dielectric materials, has been receiving significant attention in recent years because of its superior structural, chemical, and electronic properties.[1,2,4] Being a wide-band-gap ($E_g \approx 4.9$ eV) material, Ga_2O_3 finds numerous applications in optoelectronics, high power electronics, chemical sensing, dielectric coatings for solar cells, and ultraviolet transparent conductive oxide in optical devices.[3,11−13] The high breakdown field (8 MV/cm) of Ga_2O_3 offers excellent opportunities for the design and development of high power Schottky diodes and high-voltage field effect transistors.[14]

Gallium oxide exhibits five different polymorphs namely α, β, γ, δ, and ε.[15] Among the different polymorphs of Ga_2O_3, β-Ga_2O_3 is thermodynamically more stable from ambient to until its melting point, whereas other polymorphs α, γ, δ, and ε are metastable and transforms into β phase at sufficiently high temperatures in air. The order of formation energies for different polymorphs is $\beta < \varepsilon < \alpha < \delta < \gamma$. The crystal structure of β-Ga_2O_3 is a base-centered monoclinic (space group $C2/m$), where the oxygen ions sit in a distorted cubic packing arrangement and Ga^{3+} sits in distorted tetrahedral and octahedral sites.[15] The lattice parameters of β-Ga_2O_3 are a = 12.23 ± 0.02 Å, b = 3.04 ± 0.01 Å, c = 5.80 ± 0.01 Å, and β = 103.7 ± 0.3°.[16] Intrinsic β-Ga_2O_3 behaves as an insulating oxide at room temperature but exhibits n-type semiconducting behavior at high temperatures.[17] Being thermally and chemically stable oxide, β-Ga_2O_3 is well known for its functionality at extreme environments.[18−20] In view of fascinating properties and potential technological applications in diverse fields, Ga_2O_3 has been studied extensively. Several research groups have paid attention to tune their structural and physical properties by various means, such as elemental doping, adopting different processing methods, and fabricating thin films using different techniques.[18,21,22] Specifically, in order to further improve the functionality and performance of Ga_2O_3, doping using either isovalent and/or multivalent ion(s) has been considered in the literature.[23,24] There are only a few

Received: August 14, 2018
Revised: October 16, 2018
Published: October 22, 2018

DOI: 10.1021/acs.jpcc.8b07921
J. Phys. Chem. C 2018, 122, 27597−27607

theoretical/experimental studies which discuss about possible defects and effect of these defects on n-type conductivity of Ga_2O_3 upon doping of transition metals. Effect on n-type conductivity by doping of transition metals such as W, Mo, Re, and Nb in Ga_2O_3 is discussed based on formation energies using first-principles calculations.[25] All these impurities or dopants can be incorporated at Ga sites in inequivalent crystallographic sites, with preferentially in octahedral sites. In contrast to Fe, Mo, and Re act as deep donors, whereas tetrahedral sites of W and Nb act as shallow donors with a difference in formation energies. Zn and Cu act as acceptors, these dopants increase hole concentrations in intrinsic Ga_2O_3.[20] It has been demonstrated that doping of Ga_2O_3 with tungsten (W) and titanium (Ti) provides enhanced ability to obtain tunable and controlled optical properties.[24,26] Additionally, Oleksak et al. have demonstrated that W-doped Ga_2O_3 thin films can form dense low-*k* dielectric materials, where the relative W content can significantly alter the dielectric constant.[27] The Ga_2O_3 nanowires doped with Li or In shown enhanced luminescence for application in display devices.[21,28] The enhanced photocatalytic activity, which may be useful in a wide variety of energy-harvesting devices, has been reported for transition metal ion-doped Ga_2O_3 and Ga_2O_3 hybrid materials.[22]

It is well known and evident that the nature and amount of foreign metal ions will dictate the resulting properties and phenomena of Ga_2O_3.[18,23,26] Therefore, it will be of great interest to study the doping of isovalent/aliovalent ions at Ga sites in Ga_2O_3 crystal to investigate the effect of such metal ions on structural, physical, chemical, and electronic properties of the resulting materials. Specifically, from fundamental as well as applied perspective, it is highly beneficial to derive a better understanding of the underlying science of the transition metal ion doping into Ga_2O_3 to design materials for electrical and optical device applications. In this context, the present work was performed on the effect of variable Fe content on the structural, physical, chemical, electrical, and dielectric properties of Fe-doped Ga_2O_3. While there are very limited studies of Fe-doped Ga_2O_3, the impetus for the present work is derived from the following considerations. The Shannon ionic radii Ga and Fe closely match with each other; Ga^{3+}—0.62 Å (octahedral coordination), 0.47 Å (tetrahedral coordination) and Fe^{3+}—0.64 Å (octahedral coordination), 0.49 Å (tetrahedral coordination).[1,29] It is reasonably assumed that Fe^{3+} can be substituted to Ga sites and can replace Ga^{3+} from both octahedral and tetrahedral positions in stoichiometric proportion. However, isovalent Fe^{3+} may induce some degree of structural disorder and lattice strain, which can significantly modify the electrical and dielectric properties in comparison to those of intrinsic β-Ga_2O_3. Also, the physical and chemical properties of the doped Ga_2O_3 are sensitive to the microstructure and chemistry, which in turn depends on the synthesis process and conditions employed. We recently reported the effect of thermochemical synthetic conditions and have demonstrated optimum conditions to obtain phase pure (single phase) Fe-doped Ga_2O_3 by the standard solid state chemical reaction method.[1] It is well known that X-ray absorption near edge structure (XANES) is more efficient in determining the changes at local geometries and electronic structure of compounds. XANES is a very sensitive technique, which can determine changes in coordination geometry and oxidation states of constituent elements of the complex chemical compounds.[30,31] On the basis of the results obtained, a correlation between chemical composition, crystal structure, density, microstructure, and dielectric properties of Fe-doped Ga_2O_3 is established.

2. EXPERIMENTAL DETAILS

2.1. Synthesis. $Ga_{2-x}Fe_xO_3$ (GFO, x = 0.00−0.30) compounds were prepared using a conventional solid-state chemical reaction method. High pure (99.99%) precursor materials, Ga_2O_3 (Sigma-Aldrich) and Fe_2O_3 (Noah Technologies Corporation), were used to obtain phase pure GFO compounds. Ga_2O_3 and Fe_2O_3 compounds were weighed in stoichiometric proportion in accordance to specific concentration. The stoichiometrically weighed compounds were grounded in an agate mortar to obtain homogeneously mixed compound using ethanol as a wetting media. The homogenously mixed powders were calcined at 1100 °C for 6 h in a muffle furnace with a ramp rate of 10 °C/min (heating and cooling). The calcined powders were again grounded to reach ultrafine particles with narrow particle size distribution, which helps to improve the sintering ability of pellets. The circular pellets (8 mm diameter and 2 mm thickness) were made using uniaxial hydraulic press by applying 5 ton load. The as-prepared pellets were sintered at 1200 °C for 6 h in the same muffle furnace to fabricate final pellets with superior density.

2.2. Crystal Structure and Morphology. The phase purity and crystal structure of synthesized GFO compounds were studied using a Bruker D8 Discover X-ray diffractometer (Source: Cu Kα, λ = 1.5406 Å). The lattice constants (a, b, c), unit cell volume (V) and theoretical density (ρ_{th}) were calculated from the X-ray diffraction (XRD) data. The magnitude of error while calculating the lattice constants is about 0.0004 Å which is negligible. The following equations (eq 1−3) are employed for cell parameters, unit cell volume, and density calculations:[1]

$$1/d^2 = 1/\sin^2\beta(h^2/a^2 + k^2\sin^2\beta/b^2 + l^2/c^2 - 2hl\cos\beta/ac) \quad (1)$$

$$V = abc\sin\beta \quad (2)$$

$$P_{th} = nM/NV \quad (3)$$

where M is the molecular weight, N is the Avogadro number, n is the number of atoms per unit cell (here, n = 2), and V is the unit cell volume. Surface morphology of the GFO samples was studied using a Hitachi S-4800 field emission scanning electron microscope (SEM) operating in secondary electron imaging mode at an applied source voltage of 20 kV.

2.3. Chemical Analysis. *2.3.1. Energy Dispersive X-ray Spectroscopy (EDS).* The EDS spectra were collected to confirm the stoichiometry of synthesized compounds. In addition, elemental mapping was carried out for the samples to observe the constituent element distribution. Prior to imaging, samples were coated with gold to avoid the charging effect.

2.3.2. X-ray Absorption Near-Edge Structure. The XANES spectra of sintered powders were collected at beamline 6.3.1.2 of the advanced light source (ALS) in total electron yield mode. To collect the patterns, the specimen powders were pressed into In foil and fixed onto a Cu sample puck using adhesive carbon tape. The analysis chamber pressure was maintained below 1×10^{-9} Torr during the measurements. Calibration standards were furnished by ALS mounted within

DOI: 10.1021/acs.jpcc.8b07921
J. Phys. Chem. C 2018, 122, 27597−27607

the X-ray absorption spectroscopy instrument chamber for accurate measurement of the energy positions.

2.4. Dielectric Properties. Dielectric measurements were performed using a HP precision LCR meter. Prior to the measurements, samples were fine polished and coated with silver paste on both sides. Silver-coated pellets were cured at 90 °C for 2 h to make sure the proper functioning of the electrodes. For all the samples, capacitance and dielectric dissipation (tan δ) data were collected to calculate the real (ε') and imaginary (ε'') parts of the dielectric constant. Data are collected in the frequency range of 90 Hz to 1 MHz at 1 V input ac signal amplitude. High temperature measurements were performed at 1 KHz, 10 KHz, 100 KHz, and 1 MHz, respectively, employing a temperature-controlled furnace. The temperature was varied from 30 to 500 °C.

3. RESULTS AND DISCUSSION

3.1. Crystal Structure and Morphology. Figure 1 shows the XRD patterns of selected GFO compounds. There is no discernible difference noticed for differently doped GFO compounds. The XRD patterns clearly indicate that the intrinsic Ga_2O_3 and GFO compounds crystallize in monoclinic phase with $C2/m$ space group ((JCPDS #00-041-1103).[32] The peaks and their respective positions are as indexed in Figure 1. The XRD patterns confirm the phase purity of the GFO compounds, where no sign of secondary phase is even at a relatively higher Fe content. As anticipated, a clear solid solution is formed because of close ionic radii of Ga^{3+} and Fe^{3+} in both tetrahedral and octahedral coordination.

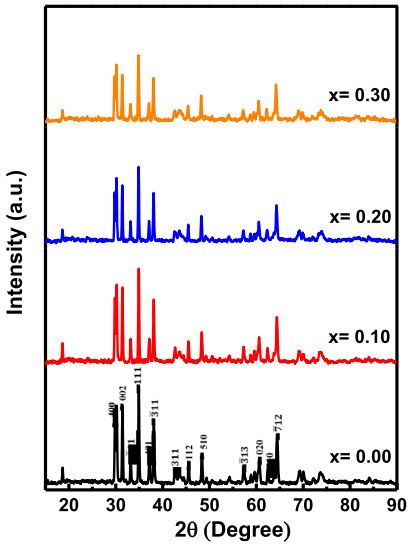

Figure 1. XRD pattern of GFO compounds.

The unit cell parameters of pure Ga_2O_3 and GFO compounds were calculated by the procedure outlined in previous section. The cell parameter values of GFO compounds are summarized in Table 1. The unit cell parameters of intrinsic Ga_2O_3 are in agreement with the literature.[33] Along with the cell parameters of GFO solid solutions, the data obtained on physical properties are also presented in Table 1. Effective density (ρ_{eff}) of the GFO samples was calculated employing Archimedes principle (ASTM B962). Relative porosity was calculated by comparing theoretical density (ρ_{XRD}) and ρ_{eff}.[1] It is evident (Table 1) that the cell parameters increase with increasing Fe content because of slightly higher ionic radius of Fe^{3+} compared to Ga^{3+}. Also, because of the thermal processing of the compounds, lattice distortion might have taken place because of the difference in thermal expansion co-efficient. We can observe that, with increasing iron concentration, the lattice constant mismatch between the intrinsic Ga_2O_3 and GFO compounds increases slightly. It is known that intrinsic Ga_2O_3 has inherent oxygen vacancies and atomic oxygen can be introduced in the pellets from the furnace atmosphere at high processing temperatures.[1] This atomic oxygen then converts into the molecular oxygen, which remains in the GFO defect structure, causing lattice distortion which may lead to slight increment in the unit cell parameter and consequently peak angle shifts in XRD pattern. Figure 2 shows the variation of theoretical density (ρ_{XRD}) with increasing Fe concentration. The measured effective density (Table 1) of the pellets is lower than the theoretical density.

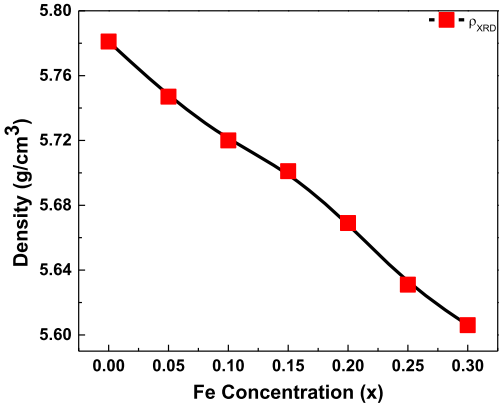

Figure 2. Variation of the theoretical density (ρ_{XRD}) of GFO compounds with Fe content. The unit cell volume values were determined from the XRD measurements.

Table 1. Lattice Constant, Unit Cell Volume, Density, and Relative Porosity of GFO Compounds

dopant concentration (x)	lattice parameter (Å)			unit cell volume V (Å^3)	theoretical density ρ_{th} (g/cm^3)	effective density ρ_{eff} (g/cm^3)	relative porosity (%)
	a	b	c				
0.00	12.405	3.052	5.897	215.323	5.781	3.766	26.55
0.05	12.396	3.053	5.893	215.320	5.717	3.741	34.56
0.10	12.410	3.053	5.892	215.478	5.709	3.656	35.96
0.15	12.415	3.056	5.896	215.929	5.701	3.629	36.34
0.20	12.429	3.056	5.901	216.329	5.669	3.624	36.07
0.25	12.450	3.057	5.910	216.946	5.631	3.590	36.25
0.30	12.452	3.059	5.909	217.116	5.606	3.570	36.32

DOI: 10.1021/acs.jpcc.8b07921
J. Phys. Chem. C 2018, 122, 27597−27607

These lower values of the effective density (ρ_{eff}) depend on many factors such as duration of sintering process and presence of porosity and/or atomic scale defects, which is unavoidable in this kind of high-temperature ceramic synthesis process.[31,32] The calculated relative porosity is more or less same for all the pellets and is around 36% except for pure Ga_2O_3 which is 26.55%.

The crystallite size of the GFO compounds was calculated using the Scherrer formula[33]

$$\beta s = \lambda / D \cos \theta \quad (4)$$

where D is the average crystalline size, λ is the wavelength of Cu Kα radiation (1.5406 Å), θ is the Bragg's angle, and βs is the measured integral width of the peak. The integral width was calculated by multiplying with the shape factor (dimensionless). Gaussian function was used to calculate the full width at half maximum (FWHM) of the peaks.[34] The variation of average crystallite size with Fe concentration was in the range of 57−62 nm. Thus, there is no considerable change in crystallite sizes with varying Fe concentration.

Figure 3 shows the SEM images of GFO compounds. Fe doping moderately changes the microstructure of intrinsic

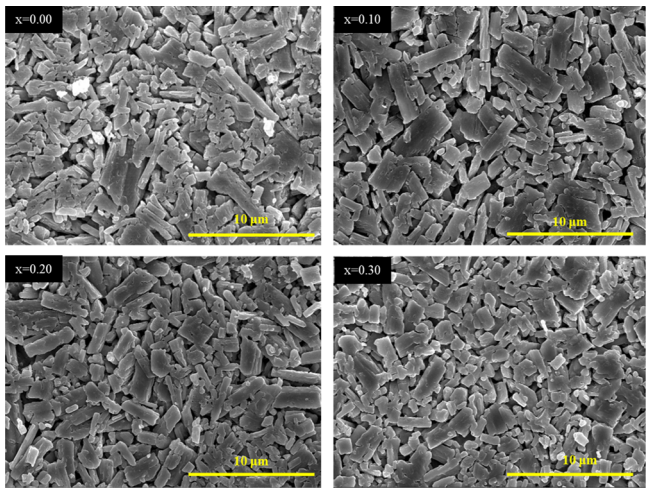

Figure 3. SEM data of $Ga_{1-x}Fe_xO_3$ compounds.

Ga_2O_3. The rod-shaped particle morphology is observed in all the sintered samples. The rod-shaped morphology is the inherent characteristic of Ga_2O_3, which is also reported by Shimura and Yoshida.[22] The particle coalescence can be seen in some cases predominantly in higher Fe content samples. The particle size reduction from 3.5 to ∼2.0 μm with increasing Fe content can be noticed. The particle size is measured by employing ImageJ software analysis with at least 30 measurements per sample. An interesting phenomenon observed is the narrow particle size distribution with increasing Fe doping. Smooth and uniform distribution of the particles can be noticed in all images that is one of the characteristics of the high-temperature solid state synthesis process. Also, it is helpful in getting better final densification through the sintering process.

The rod-shaped particle feature seen throughout the microstructures of all the four GFO compounds correlates our observation with the XRD and lately with XANES studies, where it is mentioned that the doped Fe preferentially sits in the parental Ga sites by forming substitutional solid solutions and maintains the same crystal symmetry as of the intrinsic Ga_2O_3. Thus, the salient characteristic features of the Ga_2O_3 can only be expected and seen in the SEM images rather than the features corresponding to the doped iron or iron oxide compounds. The apparent larger particles seen in the less iron containing samples might be due to the coalescence of the smaller particles. Integration and annexation phenomena between grains become obvious at the optimized processing condition. As a result of these, most of the voids and/or holes present in the material before were starting to disappear, paving the way for continuous grain growth.[34] Atuchin et al. and Lim et al. have also observed similar behavior in Mo- and Ge-containing multicomponent oxide ceramics.[35−38] Fe doping in pure Ga_2O_3 might help in the formation of smaller nuclei and inhibit the grain growth during the synthesis and sintering process respectively. It might act as a kinetic barrier which prevents further grain displacement and segregation throughout the microstructure, thus reducing further grain growth.[39,40] Although from the XRD and XANES studies it can be concluded that most of the doped Fe ions occupied the substitutional lattice positions of the parental Ga ions owing to their same ionic radii, some fractions can fit itself in the defect chemistry and/or in the interstitial lattice positions and impede the grain growth process.

Discussion on defects, specifically line or point defects in the lime light of SEM, is not totally possible because of the inherent low resolution of the SEM instruments. However, it is reliable to comment on the grain boundaries and qualitatively on the microscopic porosity of the micrographs. It is evident from the SEM images that some pores are present in each of the micrographs and it can be supported by our porosity calculations, though no typical characteristic grain boundary is omnipresent throughout the micrographs. From Table 1, it is obvious that the relative porosity percentage increases for the GFO compounds in comparison to the pure β-Ga_2O_3 by more or less 10%, but among the GFO compounds, it is almost constant (∼36%). As mentioned before that, with increasing Fe concentration, the rod-shaped particles take narrow size distributions and probably this has helped to restrain the porosity level to a legitimate range. It can be assumed by the visual observation of the micrographs that higher Fe content GFO compounds have more compact structure. However, pure Ga_2O_3 micrograph has also evidenced a close-packed structure. This can be attributed to the Fe doping which might act as the grain growth inhibitor helped to obtain a narrow size distribution of the particles throughout the micrographs. In case of solid-state processing, porosity can act as a pinning phase and hinder grain growth. Liu and Patterson described elaborately on how porosity as a dispersed second phase in the main matrix can act as a grain growth inhibitor and help in achieving proper densification.[41] Porosity can be like interconnected channels or segregated upon separation based on the sintering conditions. It reduces the total energy of the grain boundary by getting attached to it and consequently slows down the grain boundary movement. Parameters such as effective surface area of pores, contact area between the pore and the grain boundary, grain boundary curvature, as well as the relative motion between the grain boundary and pore influence the above discussed phenomenon.[41]

3.2. Chemical Analysis. It is evident from the EDS data (Figure 4) that the dispersion of the constituent cations, that is, the ratio of Fe to Ga, is properly maintained closer to the theoretical atomic ratio despite the fact that the high temperature fabrication route is adopted to synthesize these

DOI: 10.1021/acs.jpcc.8b07921
J. Phys. Chem. C 2018, 122, 27597−27607

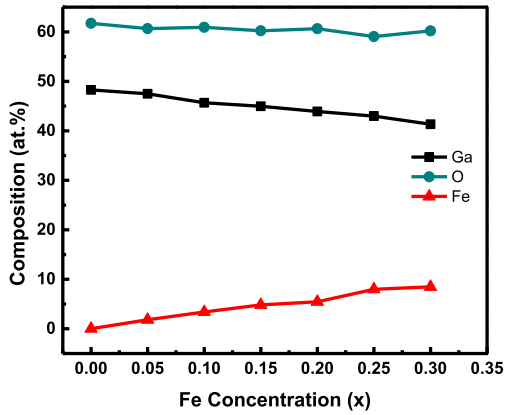

Figure 4. Atomic ratio of constituent elements of GFO compounds obtained from EDS.

samples. The EDS analysis of samples confirms that, in sintered samples, the constituted elements are in stoichiometric proportion with respect to desired composition. We attribute this chemical quality of the GFO samples due to proper mixing of the constituents during the preparation stages, precise maintenance of the furnace atmosphere by controlling the associated parameters, and exact densification obtained by employing the optimum firing conditions.[27]

The elemental composition data collected from EDS are presented in Figure 4. It can be seen that the Ga content in GFO compounds decreases progressively with increasing Fe content. Figure 5 shows the elemental mapping of pure Ga_2O_3 and with highest Fe content (x = 0.30) GFO compound. It is evident from these images that the Fe-doped Ga_2O_3 compounds are homogeneous in terms of distribution of the principal constituent elements. The images report the increasing amount of iron which is noticeable from the image color contrast and the chemical homogeneity throughout the samples. Such chemical homogeneity is noted in all the GFO compounds.

3.3. Local Structure and Bonding. The XANES data of GFO compounds with Ga_2O_3 structural figure are shown in Figure 6. The data shown in Figure 6a–c are the Ga L-edge, Fe L-edge, and O K-edge spectra, respectively, obtained as a function of variable Fe content. Figure 6d depicts the tetrahedral (Ga1) and octahedral (Ga2) coordination positions in the Ga_2O_3 structure. The as-received Ga_2O_3 and Fe_2O_3 powders were used as the reference samples. From this observation, it is evident that GFO compounds crystallized in beta monoclinic phase without any structural modification even at higher content of Fe. In intrinsic Ga_2O_3, Ga^{3+} occupies both octahedral and tetrahedral lattice positions.[22] Ga L-edge spectra (Figure 6a) show two absorption peaks at around 1120 and 1128 eV. The first peak at 1120 eV arises due to octahedral coordination of Ga^{3+} (circled as O), whereas the second peak at 1128 eV is for tetrahedral coordination (circled as T). However, there is no considerable variation in Ga L-edge absorption spectra even at higher concentration of Fe, but small shift in absorption peaks attributed to change in bond length because of the slight ionic radii difference of Ga^{3+} and Fe^{3+}.

The O K-edge (Figure 6b) XANES spectra are different from the Ga L-edge XANES spectra for GFO compounds. Two peaks at around 535 and 542 eV can be observed for O K-edge, which is the characteristic of β-Ga_2O_3.[29,35,36] A broad diffused peak can be seen for Ga_2O_3 powder sample, which is absent in spectra of the GFO samples. This pre-edge feature can be attributed to the presence of ε-Ga_2O_3, as commercial Ga_2O_3 powder generally is a mixture of ε-Ga_2O_3 and β-Ga_2O_3.[31]

The Fe L-edge (Figure 6c) spectra show one absorption band, that is, around 710 eV and the other absorption band, which is around 722 eV, is not shown here. The two absorption features are corresponding to L3-edge and L2-edge (circled in Figure 6c as for L3), respectively, which are separated due to core–hole and 3d orbital interactions.[29] These absorption features are in good agreement with the literature of α-Fe_2O_3. Moreover, the splitting of L3-edge is due to crystal field splitting of 3d orbital interactions.[29,30]

The inherent defects in intrinsic β-Ga_2O_3 are the oxygen vacancies and Ga interstitials.[15,42] The defect concentration in intrinsic β-Ga_2O_3 is directly associated with the electron concentration, and a theoretical relation between the electron concentration and oxygen partial pressure has been established which is $[é] \approx pO_2^{-1/4}$, where [é] denotes the electron concentration and pO_2 indicates the partial pressure of oxygen.[15] Intrinsic gallium oxide has three different oxygen configurations, and these configurations vary for different charged states. While one of the oxygen atoms is arranged in tetragonal configuration, the rests of the three are coordinated trigonally. Gallium also has two configurations namely tetrahedral and octahedral in the β-Ga_2O_3 crystal system.[15,43] It is not clear that which site is more energetically favorable though some researchers favor the tetragonal site as the energetically lower site for maintaining the crystal symme-

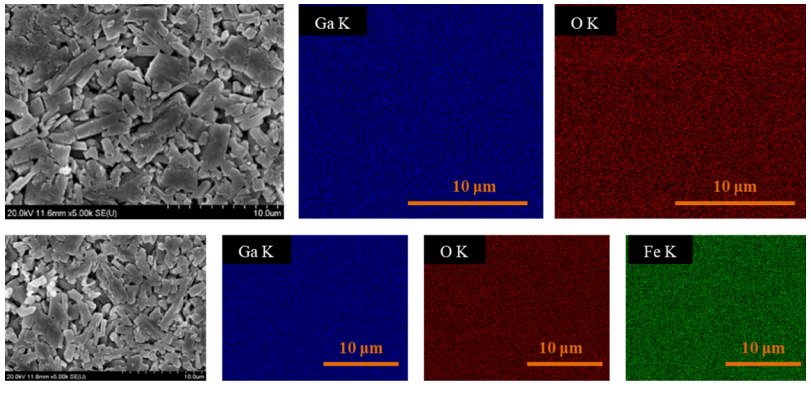

Figure 5. Elemental mapping of representative GFO compounds. The data indicate the uniform distribution of the constituent elements.

DOI: 10.1021/acs.jpcc.8b07921
J. Phys. Chem. C 2018, 122, 27597–27607

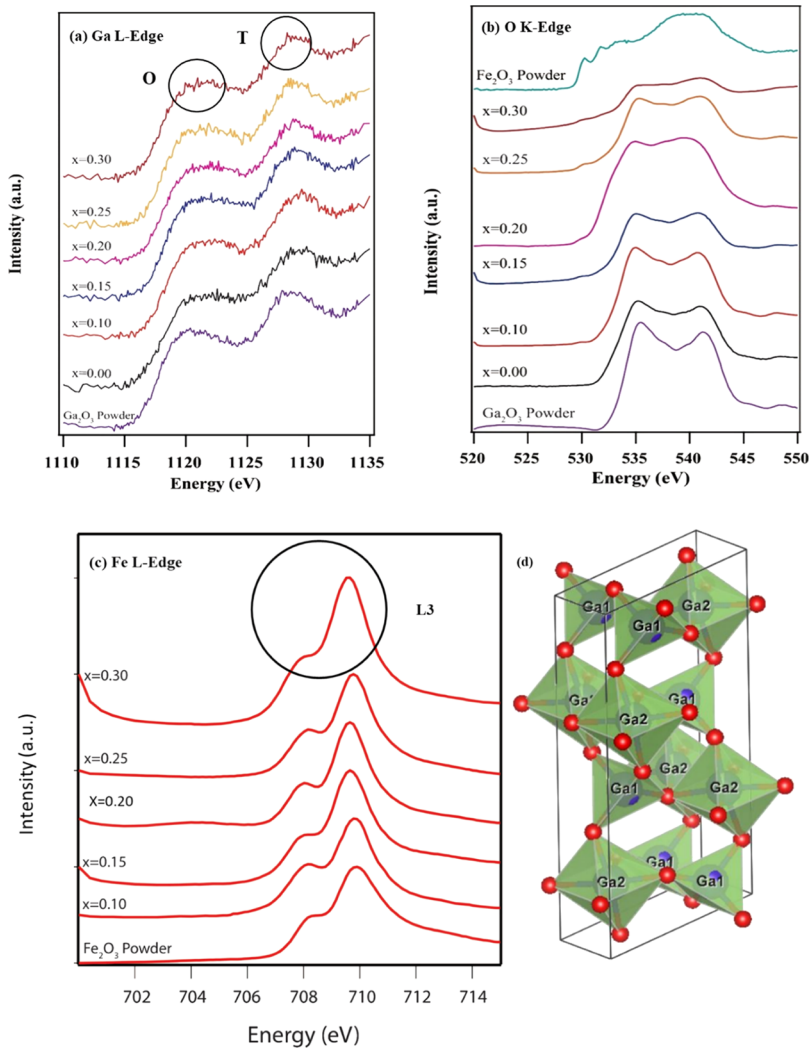

Figure 6. XANES of (a) Ga L-edge, (b) O K-edge, (c) Fe L-edge, and (d) representative crystal structure of Ga_2O_3 with tetrahedral and octahedral coordination positions. Ga1 and Ga2 denote the tetrahedral and octahedral lattice sites in pure Ga_2O_3 compound, respectively. Oxygen atoms at their respective positions are represented by red circles.

try.[42,44] Inherent defect concentration is so small in intrinsic β-Ga_2O_3 that introducing small amounts of foreign element can alter the defect chemistry.

It is argued that the negative charge defects have higher formation energy than the positive charge defects. The formation energy of the oxygen vacancies is lower than the gallium interstitials but often oxygen vacancies are considered as the deep donors (i.e., deep transition levels) and responsible for the n-type conductivity, whereas other researchers cited that the charge carrying ability of the intrinsic β-Ga_2O_3 oxide is solely due to the defect complexes of hydrogen atom which is a shallow donor.[43,45] Being a direct band gap material, the band structure of β-Ga_2O_3 exhibits a flat valence band, indicating a high concentration of holes which leads to the low hole mobility, and this self-localization of holes became the main barrier in the fabrication of p-type β-Ga_2O_3 by doping foreign elements.[45]

The formation energy of oxygen vacancies strongly depends on the chemical potential of oxygen and the Fermi energy. The chemical potential of oxygen is not a fixed value and changes with the different ambient atmospheric conditions. The oxygen vacancies become the defects with lowest formation energy under oxygen deficient conditions and vise-versa. Defects associated with oxygen vacancies are more stable in their fully charged states.[43,45] For low monoclinic symmetry compounds, a large number of different point defects (e.g., Frenkel, anti-Frenkel and Schottky) have to be considered.[43] The associated equations for the inherent β-Ga_2O_3 defects are as follows:

$$Ga^{\times} \leftrightarrow V_{Ga}^{\prime\prime\prime} + Ga_i^{\bullet\bullet\bullet} \quad (5)$$

$$O^{\times} \leftrightarrow V_O^{\bullet\bullet} + 2e' + 1/2O_2(gas) \quad (6)$$

where $Ga^{\times}$ denotes the neutral Ga positions in Ga_2O_3 crystal, $V_{Ga}^{\prime\prime\prime}$ denotes the gallium vacancy, $Ga_i^{\bullet\bullet\bullet}$ denotes the gallium interstitials, $O^{\times}$ denotes the neutral oxygen positions, and $V_O^{\bullet\bullet}$ denotes the oxygen vacancy and e′ denotes the electron. These defects play a very significant role under high temperature conditions in association with lattice vibration and phonon dispersion. It has been found as a general behavior that the negatively charged defects such as $V_{Ga}{}^{\prime\prime\prime}$ and $O_i{}^{\prime\prime}$ exhibited large positive relaxation volumes, whereas the positively charged defects such as $Ga_i^{\bullet\bullet\bullet}$ and $V_O^{\bullet\bullet}$ exhibited negative and smaller relaxation volumes.[46]

Density functional theory (DFT) provides the formation energy of oxygen defects in β-Ga_2O_3 with a charge state is given by[45,47]

DOI: 10.1021/acs.jpcc.8b07921
J. Phys. Chem. C 2018, 122, 27597−27607

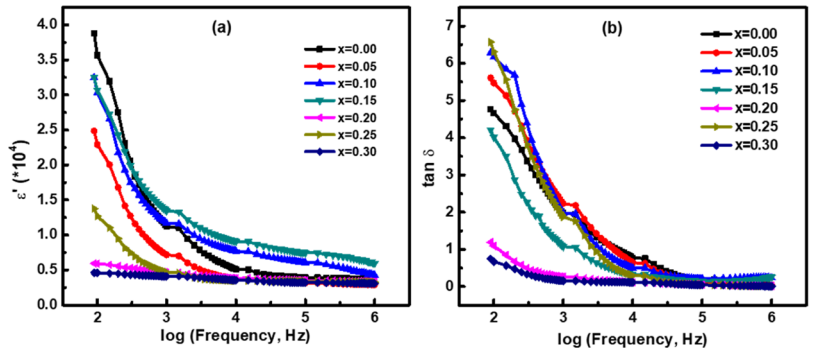

Figure 7. (a) Frequency-dependent real part of dielectric constant and (b) frequency dependent dissipation factor (tan δ) of GFO compounds.

$$E^{f}[V_O^q] = E_{tot}[V_O^q] - E_{tot}[Ga_2O_3] + \mu_O + q\epsilon_f \quad (7)$$

where $E_{tot}[V_O^q]$ and $E_{tot}[Ga_2O_3]$ represent the total energy of the supercell containing a vacancy in charge state q and perfect crystal in the same unit cell, μ_O is the chemical potential, and ϵ_f is the Fermi level measured from top of valance band. According to DFT calculations, defect formation energies vary with the Fermi level; hence, when Fermi level is close to valance band, charged oxygen defects are dominant whereas, neutral defects are dominant as the Fermi level is moving up. In GFO compounds, Fe does not form any intrinsic defect by itself, because Ga is substituted by Fe due to their close ionic radii on octahedral and tetrahedral sites and isovalent electron configuration, but Fe ions can also sit into the same interstitial defect sites as Ga^{3+}. Thus, this will maintain the almost same inherent defect structure of the intrinsic β-Ga_2O_3. A recent theoretical study reveals that Fe substituted on the octahedral Ga site (Fe_{GaII}) has high formation energy, whereas Fe substituted at tetrahedral site (Fe_{GaI}) exhibits a low formation energy. In both configurations, Fe acts as a deep acceptor level below the conduction band maximum.[47] These structural studies indicate that the doping with transition metal, especially magnetic Fe, can introduce some new characteristic features, which may allow tuning magnetic and electronic properties that can exploited in numerous electrical, optical, and optoelectronic applications, which is currently being studied.

3.4. Dielectric Properties. Figure 7 shows the real part (ε') of the dielectric constant (Figure 7a) and the dissipation factor (tan δ) (Figure 7b) as a function of frequency. The dispersion behavior of real part of the dielectric constant is the characteristic of traditional dielectric oxides. Dielectric materials exhibit high dielectric constant values at low frequencies, gradually decreases with increasing frequency. High dielectric constant at low frequencies is attributed to the extrinsic (space charge, grains, and grain boundaries) and the intrinsic contribution (ionic, dipolar, and electronic) to the dielectric polarization. Decrement of dielectric constant with increasing frequency is due to relaxation of extrinsic factors. However, predominantly, high dielectric constant at low frequencies might be attributed to the Maxwell–Wagner type of interfacial polarization.[48]

Dielectric factor (tan δ) represents the measurement of energy loss and is expressed as tan $\delta = \varepsilon''/\varepsilon'$, where angle δ is the phase difference between applied electric field and current and ε'' is the imaginary part of the complex dielectric constant. Frequency dependence has profound influence on dielectric loss values.[49,50] When polarization lags behind the applied alternating field, dielectric loss occurs. This mainly arises due to the influence of grain boundaries, impurities (e.g., doping), and crystalline defects. Density of ceramic materials also plays a key role in manipulating dielectric loss. The low-density ceramic material has high porosity which is responsible for low dielectric constant and higher loss. As the calculated relative porosity is quite similar for all the doped compounds, then it can be inferred that the role of defect chemistry upon doping is playing a significant role in determining the trend of dielectric loss data. Though it is confirmed from the XRD and XANES studies that most of the doped Fe occupied the parental lattice positions, but some of them can occupy the interstitial positions or the other defect sites. Also, it is important to consider that the inherent defects for the intrinsic Ga_2O_3 are the interstitial Ga ions and O_2 vacancies. It is quite possible that for some specific doping concentration, the defect chemistry changes in the GFO compounds, which gives inconsistent dielectric loss data. The formation of the low dielectric phases and detachment of the loosely bound charges from the surface can also be the reasons. The dielectric loss for those particular GFO compounds is slightly higher in the low frequency region than the remaining compounds, but with increasing frequency, it can be observed that the loss components decrease exponentially as like the other compounds and tend to zero. With increasing iron doping (i.e., increasing impurity level) in Ga_2O_3 decreases this jumping tendency. This might be due to two reasons: first, due to the overpopulated charge carriers which lead to the strong interaction with the lattice and, secondly, due to the absence of major polarizing factors. It is evident from the graph (Figure 7b) that dielectric loss decreases with increasing frequency.

The modified Debye's model was used to simulate the experimentally measured dielectric constant because more than one ion (Ga^{3+}, Fe^{3+}, and O^{2-}) are involved in the relaxation process. Using this model, the observed dispersion in ε' is modeled according to

$$\varepsilon'(\omega) = \varepsilon'\infty + \left[\frac{\varepsilon'_o - \varepsilon'_\infty}{1 + (\omega\tau)^{2(1-\alpha)}}\right] \quad (8)$$

where $\varepsilon'(\omega)$ is the complex permittivity, $\varepsilon'_o - \varepsilon'_\infty$ represents the dielectric relaxation strength, ε'_o being the static (lowest frequency permittivity, 90 Hz in our case), and ε'_∞ is the permittivity at the highest frequency (1 MHz). τ is the Debye average relaxation time, α is the spreading factor of the actual relaxation time about the mean value, and the field's angular frequency ω is expressed as $\omega = 2\pi f$, where f is the linear

DOI: 10.1021/acs.jpcc.8b07921
J. Phys. Chem. C 2018, 122, 27597−27607

frequency of the applied field with a signal of 1 V. Figure 8 compares the experimental and simulated values of frequency-

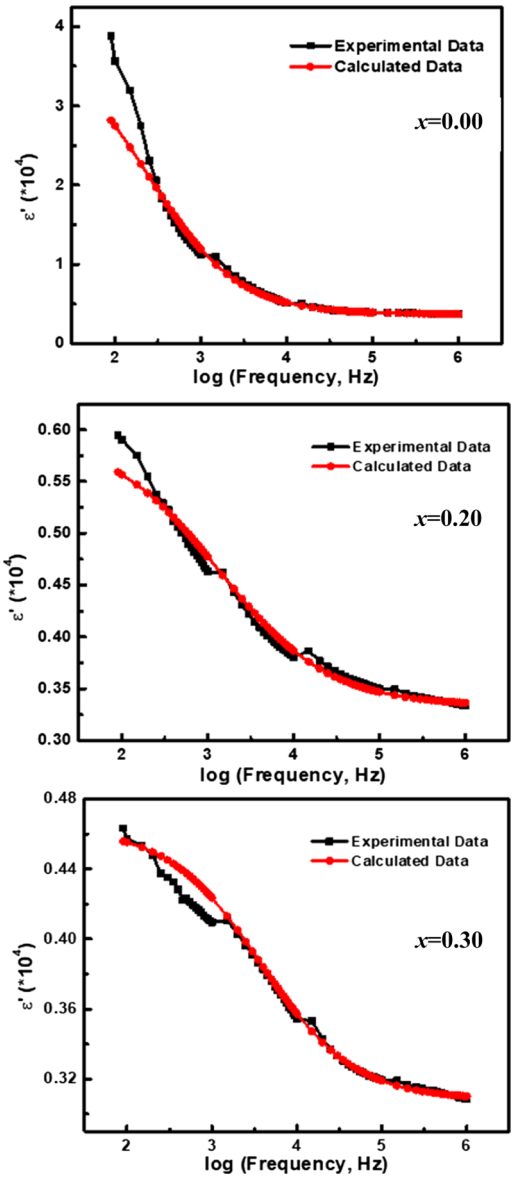

Figure 8. Variation of real part of the dielectric constant of GFO compounds with frequency. The dispersion behavior in all these plots fits to the modified Debye function.

dependent real part of the dielectric constant (ε'). With the help of the Cole−Cole plot,[50] the spreading factor for GFO compounds was obtained. However, in our modified method, real part of the dielectric constant was considered rather than the complex part, and the graph shown in Figure 9 was plotted for $\ln[(\varepsilon'_o - \varepsilon'_\omega)/(\varepsilon'_\omega - \varepsilon'_\infty)]$ versus $\ln \omega$ for all the compositions. A linear regression has been performed to calculate the slope of the lines and spreading factors "α" was obtained from these slopes of Figure 9. The estimated values of τ and α were used to correlate the experimentally obtained values of ε' with the calculated values by fitting the model, eq 5, and the result is shown in Figure 8. It is evident in Figure 8 that the experimental and the calculated data are in good agreement that confirms the above-mentioned dielectric relaxation behavior of the samples obeying the modified

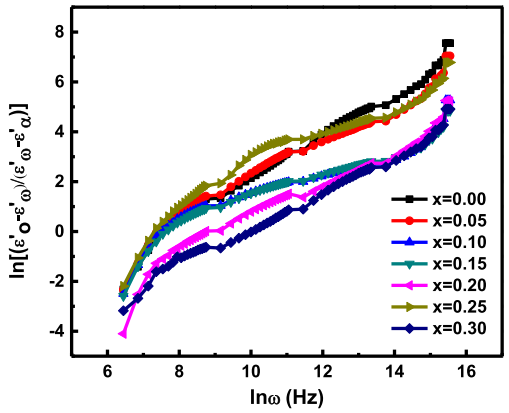

Figure 9. Variation of $\ln[(\varepsilon'_o - \varepsilon'_\omega)/(\varepsilon'_\omega - \varepsilon'_\infty)]$ vs $\ln \omega$ for GFO compounds at room temperature.

Debye model. We believe that, with increasing Fe concentration, there is a strong interaction between lattice and charge carriers. Doping Fe into Ga_2O_3 increases the interionic distance, as evidenced in structural characterization. This characteristic feature is also evident in dielectric properties, where the higher values of spreading factor and mean relaxation time with increasing Fe concentration account for increased interionic distance. Because of the higher bond length and/or interionic distance, electron hopping distance increases for Fe-doped Ga_2O_3 compounds, which, in turn, increases the α and τ values in comparison to those of intrinsic Ga_2O_3. The spreading factor values for $x = 0.00$ and $x = 0.30$ are 0.579 and 0.602, respectively. The relaxation time and the spreading factor values for the remaining compounds are calculated for the sake of simulation but are not mentioned here. The enhanced dielectric constant of some GFO compounds in comparison to Ga_2O_3 is mainly due to the extra sources of polarization because of Fe doping. This theory can be explained by the hopping of electrons between several ions that is Fe^{2+}, Fe^{3+}, Ga^{3+} and O^{2-}. This hopping of electrons facilitates the local displacement of electrons in the direction of the applied field. The dipole of the electrons thus produced orientation polarization by aligning themselves in the direction of the applied field, which subsequently increased the dielectric constant values. Iron inclusion in the Ga_2O_3 crystal system is also responsible for the rise in atomic polarizability and subsequent increment in dielectric constant. At the same time, charge accumulation at the grain boundary increased the interfacial polarization and the dielectric constant.

3.5. Effect of Temperature on the Dielectric Properties. Temperature dependence of the dielectric behavior GFO compounds has been studied in order to further understand the effect of Fe incorporation on the properties of intrinsic Ga_2O_3. The temperature-dependent plots of ε' for GFO compounds are presented in Figure 10. The data were recorded at variable frequencies in the range of 1 kHz to 1 MHz. For all the GFO compounds, dielectric constant increases monotonically with temperature at all frequencies. However, the rate of increment is higher for the lower frequencies. At the low frequency range, all types of polarizing factors, such as ionic, electronic, dipolar, and space charge, contribute to the lager values of dielectric constant. At higher frequency, ε' reaches a constant value. This might be due to the fact that at higher frequency, polarization decreases as electron hopping cannot follow the fast-changing alternating

DOI: 10.1021/acs.jpcc.8b07921
J. Phys. Chem. C 2018, 122, 27597−27607

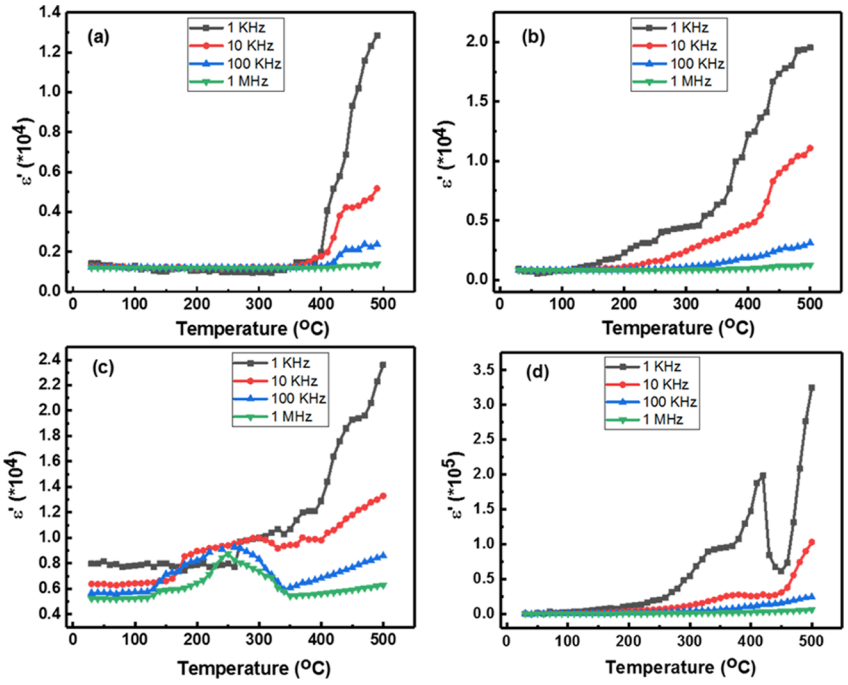

Figure 10. Variation of dielectric constant (ε') with temperature at different frequencies of the GFO compounds. (a) $x = 0.00$, (b) $x = 0.15$, (c) $x = 0.20$, and (d) $x = 0.30$.

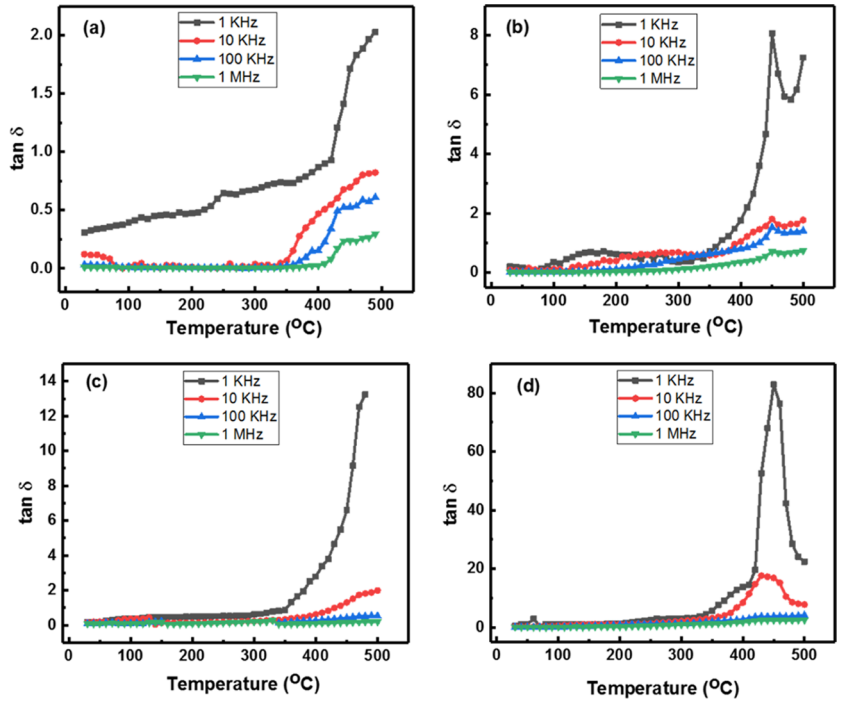

Figure 11. Variation of tan δ with temperature at different frequencies of the GFO compounds. (a) $x = 0.00$, (b) $x = 0.15$, (c) $x = 0.20$, and (d) $x = 0.30$.

current after a certain frequency level of the externally applied field. This is the reason why ε' value is almost constant for 1 MHz (Figure 10) throughout the whole temperature range. Predominantly higher dielectric constant values observed in GFO compounds at 1 kHz are attributed to the electrode material interface polarization.

Low-temperature dielectric relaxation mainly occurs due to the influence of charge carriers contributing to the interfacial polarization. At higher temperature and with increasing dopant concentration, a strong interaction between the lattice and the charge carrier occurs and due to the formation of highly insulating grain boundaries, single relaxation behavior can be noticed. Also, space charge polarization at the grain boundaries assisted by high temperature oxygen vacancies contributes to the dielectric relaxation behavior at high temperature.[51] Dielectric relaxation mechanism of a ceramic material depends on sensitive factors such as microstructural and atomic defects (e.g., porosity, Schottky and Frenkel defects), temperature,

DOI: 10.1021/acs.jpcc.8b07921
J. Phys. Chem. C 2018, 122, 27597−27607

associated electro-magnetic field, ionic substitution, relative percentage of grain and grain boundary, and so on. Incorporation of iron in pure β-Ga_2O_3 has slightly increased the interionic distance. Because of the higher bond length and/or interionic distance, electron hopping distances increase for GFO compounds.

Figure 11 illustrates the loss tangent versus temperature plot as a function of frequency for GFO compounds at different frequencies. It can be observed that tan δ increases with the increasing temperature and obtains maxima. Both temperature and frequency have profound influence on dielectric loss values.[49,52] Pure β-Ga_2O_3 exhibits low dielectric losses at different frequencies compared to the Fe-doped Ga_2O_3 compounds. Dielectric loss increases gradually with increasing temperature up to 350 °C in all the studied compositions at different frequencies. However, beyond 350 °C, dielectric loss increases drastically, and it is more predominant at low frequency (1 kHz) in the all the compositions. Dielectric loss also increases with increasing Fe concentration. The high dielectric losses at higher temperatures attributed to (a) hopping of thermally trapped electrons between different lattice sites and (b) thermally activated motion of oxygen vacancies.

4. SUMMARY AND CONCLUSIONS

Iron-doped Ga_2O_3 (GFO) compounds were synthesized employing the solid-state reaction method by varying the dopant concentration. The phase purity and crystal structure of synthesized compounds were confirmed by XRD analysis. The analysis of XRD pattern revealed that the synthesized compounds are stabilized in monoclinic phase similar to pure Ga_2O_3. Morphology of the sintered samples revealed rod-shaped particle features, and, with increasing Fe content, the particle size distribution gets narrowed down. The stoichiometry of the compounds is verified by EDS. It is evident from chemical analysis that almost each compound maintains the proper stoichiometric ratio with desired composition. XANES experiments also revealed that the doped iron species nearly equally substituted Ga^{3+} from both tetrahedral and octahedral coordinate positions. Frequency-dependent dielectric behavior of all the synthesized compounds replicates the Maxwell Wagner type dielectric relaxation at lower frequencies. Temperature-dependent dielectric data also exhibit salient characteristic features of the GFO compounds. The spreading factor values increase from about 0.58−0.60 on increasing the Fe concentration in intrinsic Ga_2O_3. The scientific understanding derived from the model system of Fe doping into Ga-oxide may be useful and can be applicable to a large class of transition metal-doped Ga_2O_3 materials.

AUTHOR INFORMATION

Corresponding Author

*E-mail: rvchintalapalle@utep.edu.

ORCID

V. Shutthanandan: 0000-0003-2957-7535

C. V. Ramana: 0000-0002-5286-3065

Notes

The authors declare no competing financial interest.

ACKNOWLEDGMENTS

The authors acknowledge, with pleasure, support from the National Science Foundation (NSF) with grant #DMR-1827745. A portion of the research (XPS measurements) was performed using Environmental Molecular Sciences Laboratory (EMSL), a national scientific user facility sponsored by the Department of Energy's Office of Biological and Environmental Research and located at Pacific Northwest National Laboratory. XANES experiments were performed at Lawrence Berkeley National Laboratory (ALS). The authors are also thankful to Sandeep Manandhar for his assistance with XANES measurements.

REFERENCES

(1) Roy, S.; Ramana, C. V. Effect of Thermochemical Synthetic Conditions on the Structure and Dielectric Properties of $Ga_{1.9}Fe_{0.1}O_3$ Compounds. *Inorg. Chem.* **2018**, *57*, 1029−1039.

(2) Comstock, D. J.; Elam, J. W. Atomic Layer Deposition of Ga_2O_3 Films Using Trimethylgallium and Ozone. *Chem. Mater.* **2012**, *24*, 4011−4018.

(3) Bartic, M.; Baban, C.-I.; Suzuki, H.; Ogita, M.; Isai, M. β-Gallium Oxide as Oxygen Gas Sensors at a High Temperature. *J. Am. Ceram. Soc.* **2007**, *90*, 2879−2884.

(4) Knapp, C. E.; Hyett, G.; Parkin, I. P.; Carmalt, C. J. Aerosol-Assisted Chemical Vapor Deposition of Transparent Conductive Gallium−Indium−Oxide Films. *Chem. Mater.* **2011**, *23*, 1719−1726.

(5) Ramana, C. V.; Utsunomiya, S.; Ewing, R. C.; Becker, U.; Atuchin, V. V.; Aliev, V. S.; Kruchinin, V. N. Spectroscopic Ellipsometry Characterization of the Optical Properties and Thermal Stability of ZrO_2 Films Made by Ion-Beam Assisted Deposition. *Appl. Phys. Lett.* **2008**, *92*, 011913−011917.

(6) Mudavakkat, V. H.; Atuchin, V. V.; Kruchinin, V. N.; Kayani, A.; Ramana, C. V. Structure, Morphology and Optical Properties of Nanocrystalline Yttrium Oxide (Y_2O_3) Thin Films. *Opt. Mater.* **2012**, *34*, 893−900.

(7) Ramana, C. V.; Vemuri, R. S.; Kaichev, V. V.; Kochubey, V. A.; Saraev, A. A.; Atuchin, V. V. X-Ray Photoelectron Spectroscopy Depth Profiling of La_2O_3/Si Thin Films Deposited by Reactive Magnetron Sputtering. *ACS Appl. Mater. Interfaces* **2011**, *3*, 4370−4373.

(8) Soliz, J. R.; Klevitch, A. D.; Harris, C. R.; Rossin, J. A.; Ng, A.; Stroud, R. M.; Hauser, A. J.; Peterson, G. W. Structural Impact on Dielectric Properties of Zirconia. *J. Phys. Chem. C* **2016**, *120*, 26834−26840.

(9) Cambiasso, J.; Grinblat, G.; Li, Y.; Rakovich, A.; Cortés, E.; Maier, S. A. Bridging the Gap between Dielectric Nanophotonics and the Visible Regime with Effectively Lossless Gallium Phosphide Antennas. *Nano Lett.* **2017**, *17*, 1219−1225.

(10) Xu, W.; Cao, H.; Liang, L.; Xu, J.-B. Aqueous Solution-Deposited Gallium Oxide Dielectric for Low-Temperature, Low-Operating-Voltage Indium Oxide Thin-Film Transistors: A Facile Route to Green Oxide Electronics. *ACS Appl. Mater. Interfaces* **2015**, *7*, 14720−14725.

(11) Fleischer, M.; Meixner, H. Gallium Oxide Thin Films: A New Material for High-Temperature Oxygen Sensors. *Sens. Actuators, B* **1991**, *4*, 437−441.

(12) Yao, Y.; Davis, R. F.; Porter, L. M. Investigation of Different Metals as Ohmic Contacts toβ-Ga_2O_3: Comparison and Analysis of Electrical Behavior, Morphology, and Other Physical Properties. *J. Electron. Mater.* **2017**, *46*, 2053−2060.

(13) Collins, P. G. Extreme Oxygen Sensitivity of Electronic Properties of Carbon Nanotubes. *Science* **2000**, *287*, 1801−1804.

(14) Yang, J.; Ahn, S.; Ren, F.; Pearton, S. J.; Jang, S.; Kim, J.; Kuramata, A. High Reverse Breakdown Voltage Schottky Rectifiers without Edge Termination on Ga_2O_3. *Appl. Phys. Lett.* **2017**, *110*, 192101.

(15) Romanov, A. E.; Stepanov, S. I.; Nikolaev, V. I.; Bougrov, V. E. Gallium Oxide: Properties and Application: AReview. *Rev. Adv. Mater. Sci.* **2016**, *44*, 63−86.

(16) Geller, S. Crystal Structure of β-Ga_2O_3. *J. Chem. Phys.* **1960**, *33*, 676−684.

DOI: 10.1021/acs.jpcc.8b07921
J. Phys. Chem. C 2018, 122, 27597−27607

(17) Korotcenkov, G. Metal Oxides for Solid-State Gas Sensors: What Determines Our Choice? *Mater. Sci. Eng. B* **2007**, *139*, 1−23.
(18) Rubio, E. J.; Mates, T. E.; Manandhar, S.; Nandasiri, M.; Shutthanandan, V.; Ramana, C. V. Tungsten Incorporation into Gallium Oxide: Crystal Structure, Surface and Interface Chemistry, Thermal Stability, and Interdiffusion. *J. Phys. Chem. C* **2016**, *120*, 26720−26735.
(19) Chen, C.-C.; Chen, C.-C. Morphology and Electrical Properties of Pure and Ti-Doped Gas-Sensitive Ga_2O_3 Film Prepared by Rheotaxial Growth and Thermal Oxidation. *J. Mater. Res.* **2004**, *19*, 1105−1117.
(20) Li, Y.; Trinchi, A.; Wlodarski, W.; Galatsis, K.; Kalantar-zadeh, K. Investigation of the Oxygen Gas Sensing Performance of Ga_2O_3 Thin Films with Different Dopants. *Sens. Actuators, B* **2003**, *93*, 431−434.
(21) López, I.; Utrilla, A. D.; Nogales, E.; Méndez, B.; Piqueras, J.; Peche, A.; Ramírez-Castellanos, J.; González-Calbet, J. M. In-Doped Gallium Oxide Micro- and Nanostructures: Morphology, Structure, and Luminescence Properties. *J. Phys. Chem. C* **2012**, *116*, 3935−3943.
(22) Shimura, K.; Yoshida, H. Effect of Doped Zinc Species on the Photocatalytic Activity of Gallium Oxide for Hydrogen Production. *Phys. Chem. Chem. Phys.* **2012**, *14*, 2678−2684.
(23) Zhang, Y.; Yan, J.; Li, Q.; Qu, C.; Zhang, L.; Xie, W. Optical and Structural Properties of Cu-Doped β-Ga_2O_3 Films. *Mater. Sci. Eng., B* **2011**, *176*, 846−849.
(24) Rubio, E. J.; Ramana, C. V. Tungsten-Incorporation Induced Red-Shift in the Bandgap of Gallium Oxide Thin Films. *Appl. Phys. Lett.* **2013**, *102*, 191913.
(25) Peelaers, H.; Van de Walle, C. G. Doping of Ga_2O_3 with Transition Metals. *Phys. Rev. B* **2016**, *94*, 195203.
(26) Manandhar, S.; Ramana, C. V. Direct, Functional Relationship between Structural and Optical Properties in Titanium-Incorporated Gallium Oxide Nanocrystalline Thin Films. *Appl. Phys. Lett.* **2017**, *110*, 061902.
(27) Oleksak, R. P.; Stickle, W. F.; Herman, G. S. Aqueous-Based Synthesis of Gallium Tungsten Oxide Thin Film Dielectrics. *J. Mater. Chem. C* **2015**, *3*, 3114−3120.
(28) López, I.; Alonso-Orts, M.; Nogales, E.; Méndez, B.; Piqueras, J. Influence of Li Doping on the Morphology and Luminescence of Ga_2O_3 Microrods Grown by a Vapor-Solid Method. *Semicond. Sci. Technol.* **2016**, *31*, 115003.
(29) Kim, D.-Y.; Miyoshi, S.; Tsuchiya, T.; Yamaguchi, S. Electronic Defect Formation in Fe-Doped $BaZrO_3$ Studied by X-Ray Absorption Spectroscopy. *Chem. Mater.* **2014**, *26*, 927−934.
(30) Chen, L. X.; Liu, T.; Thurnauer, M. C.; Csencsits, R.; Rajh, T. Fe_2O_3 Nanoparticle Structures Investigated by X-Ray Absorption Near-Edge Structure, Surface Modifications, and Model Calculations. *J. Phys. Chem. B* **2002**, *106*, 8539−8546.
(31) Zhou, X. T.; Heigl, F.; Ko, J. Y. P.; Murphy, M. W.; Zhou, J. G.; Regier, T.; Blyth, R. I. R.; Sham, T. K. Origin of Luminescence from Ga_2O_3 Nanostructures Studied Using x-Ray Absorption and Luminescence. *Phys. Rev. B: Condens. Matter Mater. Phys.* **2007**, *75*, 125303.
(32) Dakhel, A. A. Investigation of Opto-Dielectric Properties of Ti-Doped Ga_2O_3 Thin Films. *Solid State Sci.* **2013**, *20*, 54−58.
(33) Jangir, R.; Porwal, S.; Tiwari, P.; Mondal, P.; Rai, S. K.; Ganguli, T.; Oak, S. M.; Deb, S. K. Photoluminescence Study of β-Ga_2O_3 Nanostructures Annealed in Different Environments. *J. Appl. Phys.* **2012**, *112*, 034307.
(34) Mei, X.; Wang, Y.; Chen, L.; Zhang, C.; Ma, Y.; Zeng, Y.; Jiang, Y. The Effects of Sintering Conditions on the Properties of Ga-Doped Zinc Oxide Ceramics. *Mater. Res. Innovations* **2015**, *19*, S9-306.
(35) Atuchin, V. V.; Chimitova, O. D.; Adichtchev, S. V.; Bazarov, J. G.; Gavrilova, T. A.; Molokeev, M. S.; Surovtsev, N. V.; Bazarova, Z. G. Synthesis, Structural and Vibrational Properties of Microcrystalline β-$RbSm(MoO_4)_2$. *Mater. Lett.* **2013**, *106*, 26−29.
(36) Atuchin, V. V.; Subanakov, A. K.; Aleksandrovsky, A. S.; Bazarov, B. G.; Bazarova, J. G.; Dorzhieva, S. G.; Gavrilova, T. A.; Krylov, A. S.; Molokeev, M. S.; Oreshonkov, A. S.; et al. Exploration of Structural, Thermal, Vibrational and Spectroscopic Properties of New Noncentrosymmetric Double Borate $Rb_3NdB_6O_{12}$. *Adv. Powder Technol.* **2017**, *28*, 1309−1315.
(37) Atuchin, V. V.; Gavrilova, T. A.; Gromilov, S. A.; Kostrovsky, V. G.; Pokrovsky, L. D.; Troitskaia, I. B.; Vemuri, R. S.; Carbajal-Franco, G.; Ramana, C. V. Low-Temperature Chemical Synthesis and Microstructure Analysis of GeO_2 Crystals with α-Quartz Structure. *Cryst. Growth Des.* **2009**, *9*, 1829−1832.
(38) Lim, C. S.; Aleksandrovsky, A. S.; Molokeev, M. S.; Oreshonkov, A. S.; Atuchin, V. V. Microwave Synthesis and Spectroscopic Properties of Ternary Scheelite-Type Molybdate Phosphors $NaSrLa(MoO_4)_3$:Er^{3+} ,Yb^{3+}. *J. Alloys Compd.* **2017**, *713*, 156−163.
(39) Chappell, J. S.; Ring, T. A.; Birchall, J. D. Particle Size Distribution Effects on Sintering Rates. *J. Appl. Phys.* **1986**, *60*, 383−391.
(40) Coble, R. L. Sintering Crystalline Solids. II. Experimental Test of Diffusion Models in Powder Compacts. *J. Appl. Phys.* **1961**, *32*, 793−799.
(41) Liu, Y.; Patterson, B. R. Grain Growth Inhibition by Porosity. *Acta Metall. Mater.* **1993**, *41*, 2651−2656.
(42) Varley, J. B.; Weber, J. R.; Janotti, A.; Van De Walle, C. G. Oxygen Vacancies and Donor Impurities inβ-Ga_2O_3. *Appl. Phys. Lett.* **2010**, *97*, 142106.
(43) Zacherle, T.; Schmidt, P. C.; Martin, M. Ab Initio Calculations on the Defect Structure of β-Ga_2O_3. *Phys. Rev. B: Condens. Matter Mater. Phys.* **2013**, *87*, 235206.
(44) Varley, J. B.; Peelaers, H.; Janotti, A.; Van De Walle, C. G. Hydrogenated Cation Vacancies in Semiconducting Oxides. *J. Phys.: Condens. Matter* **2011**, *23*, 334212.
(45) Dong, L.; Jia, R.; Xin, B.; Peng, B.; Zhang, Y. Effects of Oxygen Vacancies on the Structural and Optical Properties of β-Ga_2O_3. *Sci. Rep.* **2017**, *7*, 40160.
(46) Ágoston, P.; Albe, K.; Nieminen, R. M.; Puska, M. J. Intrinsic N-Type Behavior in Transparent Conducting Oxides: A Comparative Hybrid-Functional Study of In_2O_3, SnO_2, and ZnO. *Phys. Rev. Lett.* **2009**, *103*, 245501.
(47) Ingebrigtsen, M. E.; Varley, J. B.; Kuznetsov, A. Y.; Svensson, B. G.; Alfieri, G.; Mihaila, A.; Badstübner, U.; Vines, L. Iron and Intrinsic Deep Level States in Ga_2O_3. *Appl. Phys. Lett.* **2018**, *112*, 042104.
(48) Maxwell, J. C. Summary for Policymakers. *A treatise Electr. Magn* **1954**, *53*, 1−30.
(49) Mangalaraja, R. V.; Manohar, P.; Gnanam, F. D.; Awano, M. Electrical and Magnetic Properties of $Ni_{0.8}Zn_{0.2}Fe_2O_4$ / Silica Composite Prepared by Sol-Gel Method. *J. Mater. Sci.* **2004**, *39*, 2037−2042.
(50) Ramana, C. V.; Kolekar, Y. D.; Kamala Bharathi, K.; Sinha, B.; Ghosh, K. Correlation between Structural, Magnetic, and Dielectric Properties of Manganese Substituted Cobalt Ferrite. *J. Appl. Phys.* **2013**, *114*, 183907.
(51) Bharathi, K. K.; Ramana, C. V. Improved Electrical and Dielectric Properties of La-Doped Co Ferrite. *J. Mater. Res.* **2011**, *26*, 584−591.
(52) Bhandare, M.; Wagh, G. Electrical Properties of Cu-Substituted Prepared by Auto-Combustion Method. **2016**, *No. 2*, 7091−7098.

DOI: 10.1021/acs.jpcc.8b07921
J. Phys. Chem. C 2018, 122, 27597−27607